

Factors determining surface oxygen vacancy formation energy in ternary spinel structure oxides with zinc

Yoyo Hinuma^{1,2*}, Shinya Mine³, Takashi Toyao^{3,4}, Takashi Kamachi^{4,5}, and Ken-ichi Shimizu^{3,4}

¹ Department of Energy and Environment, National Institute of Advanced Industrial Science and Technology (AIST), 1-8-31, Midorigaoka, Ikeda 563-8577, Japan

² Center for Frontier Science, Chiba University, 1-33 Yayoicho, Inage, Chiba 263-8522, Japan

³ Institute for Catalysis, Hokkaido University, N-21, W-10, Kita, Sapporo, Hokkaido 001-0021, Japan

⁴ Elements Strategy Initiative for Catalysts and Batteries, Kyoto University, Katsura, Nishigyo, Kyoto 615-8520, Japan

⁵ Department of Life, Environment and Applied Chemistry, Fukuoka Institute of Technology, 3-30-1 Wajiro-Higashi, Higashi-ku, Fukuoka 811-0295, Japan

* y.hinuma@aist.go.jp

Abstract

Spinel oxides are an important class of materials for heterogeneous catalysis including photocatalysis and electrocatalysis. The surface O vacancy formation energy (E_{Ovac}) is a critical quantity on catalyst performance because the surface of metal oxide catalysts often acts as reaction sites, for example, in the Mars-van Krevelen mechanism. However, experimental evaluation of E_{Ovac} is very challenging. We obtained the E_{Ovac} for (100), (110), and (111) surfaces of normal zinc-based spinel oxides ZnAl_2O_4 , ZnGa_2O_4 , ZnIn_2O_4 , ZnV_2O_4 , ZnCr_2O_4 , ZnMn_2O_4 , ZnFe_2O_4 , and ZnCo_2O_4 . The most stable surface is (100) for all compounds. The smallest E_{Ovac} for a surface is the largest in the (100) surface except for ZnCo_2O_4 . For (100) and (110) surfaces, there is a good correlation, over all spinels, between the smallest E_{Ovac} for the surface and bulk formation energy, while the ionization potential correlates well in (111) surfaces. Machine learning over E_{Ovac} of all surface sites in all orientations and all compounds to find the important factors, or descriptors, that decide the E_{Ovac} revealed that bulk and surface-dependent descriptors are the most important, namely the bulk formation energy, a Boolean descriptor on whether the surface is (111), and the ionization potential, followed by geometrical descriptors that are different in each O site.

1. Introduction

Defects can significantly influence the properties of metal oxides, where the O vacancy is the most representative defect.^{1, 2} O vacancies, when intentionally or unintentionally introduced into the metal oxide structure, could strongly affect the electrical, optical, magnetic, mechanical, and catalytic properties.^{3, 4} Surface point defects substantially affect heterogeneous catalysis because O vacancies on the surface of metal oxide catalysts often act as reaction sites.^{5, 6} As a consequence, the formation energy of an O vacancy at the surface, which is denoted as E_{Ovac} in this paper, is often used as a descriptor of the catalytic activity of metal oxides.⁷⁻¹⁰

However, experimental investigations of O vacancies remain formidable tasks despite the obvious importance of research on O vacancies in the field of catalysis.^{11, 12} Highly sophisticated techniques are necessary for determination of E_{Ovac} and the evaluation of E_{Ovac} is not always possible.¹³ On the other hand, several theoretical studies on the formation of O vacancies on metal oxides have recently emerged.¹⁴⁻²⁰ The number of investigated surfaces still remains limited although a number of contributions were made to obtain E_{Ovac} values of metal oxide surfaces. Therefore, studies that comprehensively reveal the physical principles determining E_{Ovac} are highly desirable. In this sense, we have recently reported E_{Ovac} of various insulating and semiconducting simple binary oxide surfaces using DFT calculations at the same computational level and comparable structure models.²¹

The spinel structure with the composition AB_2X_4 constitutes one of the most important classes of crystalline compounds in catalysis.²²⁻²⁶ In the normal spinel structure, A and B cations occupy two different sites in their structure, namely octahedral and tetrahedral sites, without mixing. In contrast, the octahedral sites are occupied by both A and B cations in the inverse spinel structure. The spinel oxides have attracted much attention in the field of heterogeneous catalysis including photocatalysis and electrocatalysis thanks to their structure diversities where their characteristics can be tailored by choosing appropriate A and B cations.²⁷⁻²⁹ For example, Zn-based spinel oxides are used as catalysts in various CO_2 hydrogenation reactions³⁰⁻³³ and here O vacancies play significant roles.

In this paper, the E_{Ovac} for (100), (110), and (111) surfaces of eight normal zinc-based spinel oxides without mixing of cations between A and B sites, namely ZnM_2O_4 where M is the B-site cation and is one of Al, Ga, In, V, Cr, Mn, Fe, or Co, were evaluated and the existence or non-existence of correlations with other physical quantities were investigated.

2. Computational methods

First-principles calculations were conducted using the projector augmented-wave method³⁴ as implemented in the VASP code^{35, 36}. The PBEsol functional³⁷ was used among the generalized gradient approximations (GGAs) because it reasonably reproduces energetics and crystal structures in oxide systems³⁸, for instance, compared to the standard Perdew, Burke and Ernzerhof (PBE) functional³⁹. This work focuses on ZnM_2O_4 where M is one of Al, Ga, In, V, Cr, Mn, Fe, or Co. These compounds are experimentally known to take the normal spinel structure without exchange of species between the tetrahedral Zn and octahedral M sites^{40, 41}. Choosing normal spinel structures only avoids the problem of dealing with partial occupancies on the octahedral sites. The effective U value of U - J for the valence $3d$ states was set at 5 eV for Zn and 3 eV for V, Cr, Mn, Fe, and Co. These values are the same as in Ref.⁴². The spin states of M with a formal charge of $3+$ are high spin d^2 in V^{3+} , high spin d^3 in Cr^{3+} , high spin d^4 in Mn^{3+} , high spin d^5 in Fe^{3+} , and low spin d^6 except some undercoordinated ions at the surface that can have non-zero spin in Co^{3+} . Among these, species subject to Jahn-Teller distortion are V^{3+} and Mn^{3+} . The effect of adding the Hubbard U was considered based on Dudarev's formalism.⁴³ As the magnetic ordering and the energy difference between the different magnetic solutions are highly sensitive to the functional chosen, PBEsol+ U may not be adequate and hybrid functionals might be necessary. However, we stick to practical PBEsol+ U calculations in this study.

The highest symmetry space group type of normal spinel is $Fd\bar{3}m$ (number 227), and all surfaces of normal spinel in this space group are polar (type 3) according to Tasker's definition⁴⁴, therefore making a nonpolar slab where both surfaces are identical may appear impossible. However, it is actually possible because the surfaces are nonpolar type C in the definition by Hinuma *et al.*⁴⁵. Although it is impossible to obtain a nonpolar and stoichiometric slab by simply cleaving bulk, one can be obtained by removing half of the atoms in the outermost surfaces, for instance in a stripe pattern⁴⁶.

Defect formation (O desorption) were performed on both sides of a slab such that the slab is always nonpolar. Internal coordinates and lattice parameters were relaxed in bulk calculations, and all internal coordinates were allowed to relax while lattice parameters were fixed in slab calculations.

The surface energy E_{surf} is defined as $E_{\text{surf}} = (E_{\text{slab}} - E_{\text{bulk}})/2A$, where E_{slab} , E_{bulk} , and A are the energy of the slab without defects, the energy of the constituents of the slab when in a perfect bulk, and the area of one side of the slab respectively. The O vacancy

formation energy is defined as $E_{\text{Ovac}} = (E_{\text{removed}} - E_{\text{slab}} + 2\mu_{\text{O}})/2$, where E_{removed} and μ_{O} are the energy of the slab when two O atoms are removed (one O from each surface) and the chemical potential of the O that is removed, which is referenced to O₂ gas at 0 K, respectively. E_{surf} was calculated for both “thin” and “thick” slabs (details given in Supplementary Table SI-1), and the values for these slabs were linearly extrapolated to obtain the “fitted” E_{surf} at the zero slab thickness limit (see Ref. ²¹ for details).

The primitive cell contains 14 atoms, where there are two, four, and eight symmetrically equivalent Zn, M, and O atoms, respectively. However, the energies of ZnM₂O₄ (M = V, Cr, Mn, or Fe) are lower, compared to a ferromagnetic spin ordering, in an antiferromagnetic spin ordering when the four M atoms in the primitive cells are divided into two spin up atoms and two spin down atoms. The energy difference is 72, 16, 7, and 1 meV/formula unit for M = V, Cr, Mn, and Fe, respectively. Introducing this antiferromagnetic spin ordering by considering the up and down spin M as two distinct species lowers the space group type to $I4_1/amd$ (number 141) where the spin alternates along the *c* axis. ZnV₂O₄ is dynamically stable at this space group type. However, ZnMn₂O₄ requires further lattice distortion and is dynamically stable in the space group type $I4_1/a$ (number 88). Bulk properties of the considered structures are summarized in Table 1 together with experimentally reported band gaps (BGs). Calculations typically underestimated the BGs, although the calculated BG overestimated the experimental value in ZnAl₂O₄.

A different magnetic ordering was suggested in ZnV₂O₄ by Reehis *et al.*⁴⁷. This magnetic ordering requires 28 atoms in the primitive cell. The space group type corresponding to this magnetic ordering is $F222$ (number 22), and its formation energy is almost the same with difference of at most 16 meV/atom from the 14-atom primitive cell. Slabs for systems with antiferromagnetic trivalent atoms were obtained assuming that up-spin and down-spin cations are different species. The 14-atom primitive cell was adopted because a reasonable termination for the (110) and (111) surfaces cannot be obtained with the proposed algorithm. The magnetic ordering of slab models based on the 28-atom primitive cell is incommensurate with the periodicity of slab models based on the 14-atom primitive cell, therefore relaxation of the magnetic ordering does not happen.

Table 1. Bulk properties of ZnM_2O_4 . v , E_{bulk} , and band gap (BG) are the volume per atom, formation energy per atom, and minimum band gap, respectively. Experimentally reported BGs are also shown.

Compound	Lattice parameters			v ($\text{\AA}^3/\text{atom}$)	E_{bulk} (eV/atom)	BG (eV)	Experimental BG (eV)
	a (\AA)	c (\AA)	c/a				
ZnAl_2O_4	8.049			9.310	-2.81	4.45	3.8-3.9 ⁴⁸ 4.1-4.3 ⁴⁸
ZnGa_2O_4	8.329			10.318	-2.00	2.76	Direct 4.59 \pm 0.03, indirect 4.33 ⁴⁹
ZnIn_2O_4	8.937			12.745	-1.67	1.36	
ZnV_2O_4	5.931	8.444	1.424	10.608	-2.51	0.55	2.8 ⁵⁰
ZnCr_2O_4	5.886	8.257	1.403	10.218	-2.20	2.42	3.35 ⁵¹
ZnMn_2O_4	6.049	8.016	1.325	10.476	-2.00	0.81	1.51 ⁵² 1.58 ⁵³ 2.1 ⁵⁴
ZnFe_2O_4	5.900	8.382	1.421	10.420	-1.71	1.13	2.15 ⁵⁵ 2.316 ⁵⁶
ZnCo_2O_4	7.986			9.080	-1.56	1.89	1.82 ⁵⁷

3. Results and discussion

3.1 Convergence of surface properties

When discussing the (hkl) surface, a supercell with basis vectors $(\mathbf{a}', \mathbf{b}', \mathbf{c}')$ is considered where \mathbf{a}' and \mathbf{b}' are “in-plane vectors”. Taking $(\mathbf{a}, \mathbf{b}, \mathbf{c})$ as the basis vectors of the conventional cell, an in-plane vector $h'\mathbf{a} + k'\mathbf{b} + l'\mathbf{c}$ satisfies

$$(h', k', l') \cdot (h, k, l)^T = 0 \quad \text{The thickness of the supercell is defined as } h_{\text{cell}} = \frac{(\mathbf{a}' \times \mathbf{b}') \cdot \mathbf{c}'}{|\mathbf{a}' \times \mathbf{b}'|}$$

(length of the out-of-plane basis vector projected in the direction normal to the surface)

and the slab and vacuum thicknesses are defined as $h_{\text{slab}} = r h_{\text{cell}}$ and $h_{\text{vac}} = (1-r) h_{\text{cell}}$,

respectively, where r is the ratio of atoms remaining after atom removal from a completely

filled supercell. Supplementary Table 1 gives information on the geometry of employed slabs. We investigated the most stable termination among the (100), (110), and (111) orientations in the cubic setting (orientations are referenced to the cubic setting throughout this paper). Various surface terminations considered for ZnAl_2O_4 are shown in Supplementary Figs. SI-1-3. Fig. 1 shows the typical termination of the (100), (110), and (111) surface slabs. However, deviations in axial ratios and interaxial angles from the cubic lattice forces the proposed algorithm to make models with different terminations in some surfaces, which are given in Fig. SI-4. Moreover, a reasonable termination for the (110) surface of ZnMn_2O_4 was not generated from the algorithm. The two-fold coordinated Zn at the (100) surface was additionally tilted toward the surface to lower the surface energy except for ZnMn_2O_4 and ZnFe_2O_4 where tilting did not lower the surface energy. Table 2 shows the calculated E_{surf} , difference between the number of spin up and down electrons (spin) per supercell, ionization potential (IP), and electron affinity (EA) for slabs with two different thicknesses. The bulk-based definition in Ref. ⁵⁸ was used to obtain IPs and EAs.

Table 2. Calculated E_{surf} , difference between the number of spin up and down electrons (spin), IP, and EA. Units of spin is electron magnetic moment per cell (two surfaces).

Surface (cubic)	Compound	E_{surf} (meV/Å ²)			Spin		IP(eV)		EA (eV)	
		Fit	Thin	Thick	Thin	Thick	Thin	Thick	Thin	Thick
(100)	ZnAl ₂ O ₄	102.8	94.9	93.8	0.0	0.0	6.6	6.6	2.2	2.2
	ZnGa ₂ O ₄	85.5	79.2	78.3	0.0	0.0	6.9	6.9	4.2	4.2
	ZnIn ₂ O ₄	70.4	65.6	65.0	0.0	0.0	6.5	6.5	5.2	5.1
	ZnV ₂ O ₄	83.7	77.9	77.1	0.1	-0.1	4.3	4.4	3.7	3.8
	ZnCr ₂ O ₄	112.6	99.5	97.7	0.0	0.0	5.5	5.5	3.1	3.1
	ZnMn ₂ O ₄	56.9	46.4	44.9	0.1	0.0	5.5	5.4	4.7	4.6
	ZnFe ₂ O ₄	70.9	64.9	64.0	0.0	0.0	5.6	5.6	4.5	4.5
ZnCo ₂ O ₄	102.6	97.6	96.8	0.1	0.2	5.6	5.6	3.7	3.7	
(110)	ZnAl ₂ O ₄	134.5	126.4	124.8	0.0	0.0	6.9	6.9	2.5	2.5
	ZnGa ₂ O ₄	109.6	103.0	101.6	0.0	0.0	7.0	7.0	4.3	4.3
	ZnIn ₂ O ₄	91.9	86.7	85.7	0.0	0.0	6.5	6.5	5.1	5.1
	ZnV ₂ O ₄	94.3	103.3	105.1	0.7	0.0	4.5	4.4	3.9	3.9
	ZnCr ₂ O ₄	132.9	126.6	125.3	1.5	1.5	5.6	5.6	3.2	3.2
	ZnFe ₂ O ₄	86.6	80.8	79.6	0.0	0.0	5.7	5.7	4.5	4.5
	ZnCo ₂ O ₄	120.5	115.7	114.8	0.0	0.0	5.8	5.8	3.9	3.9
(111)	ZnAl ₂ O ₄	160.6	150.3	147.7	0.0	0.0	5.0	5.0	0.6	0.6
	ZnGa ₂ O ₄	128.2	120.2	118.2	1.3	0.6	5.9	5.9	3.1	3.1
	ZnIn ₂ O ₄	94.1	88.3	86.8	0.6	0.6	6.1	6.1	4.7	4.7
	ZnV ₂ O ₄	95.4	84.2	81.4	4.0	4.0	3.6	3.6	3.0	3.0
	ZnCr ₂ O ₄	128.1	119.7	117.6	0.0	0.0	4.4	4.4	1.9	1.9
	ZnMn ₂ O ₄	78.2	70.8	68.9	4.0	4.0	4.1	4.1	3.3	3.3
	ZnFe ₂ O ₄	94.4	86.5	84.5	0.0	0.0	4.8	4.8	3.7	3.7
ZnCo ₂ O ₄	120.9	112.9	111.0	4.0	4.0	4.6	4.6	2.7	2.7	

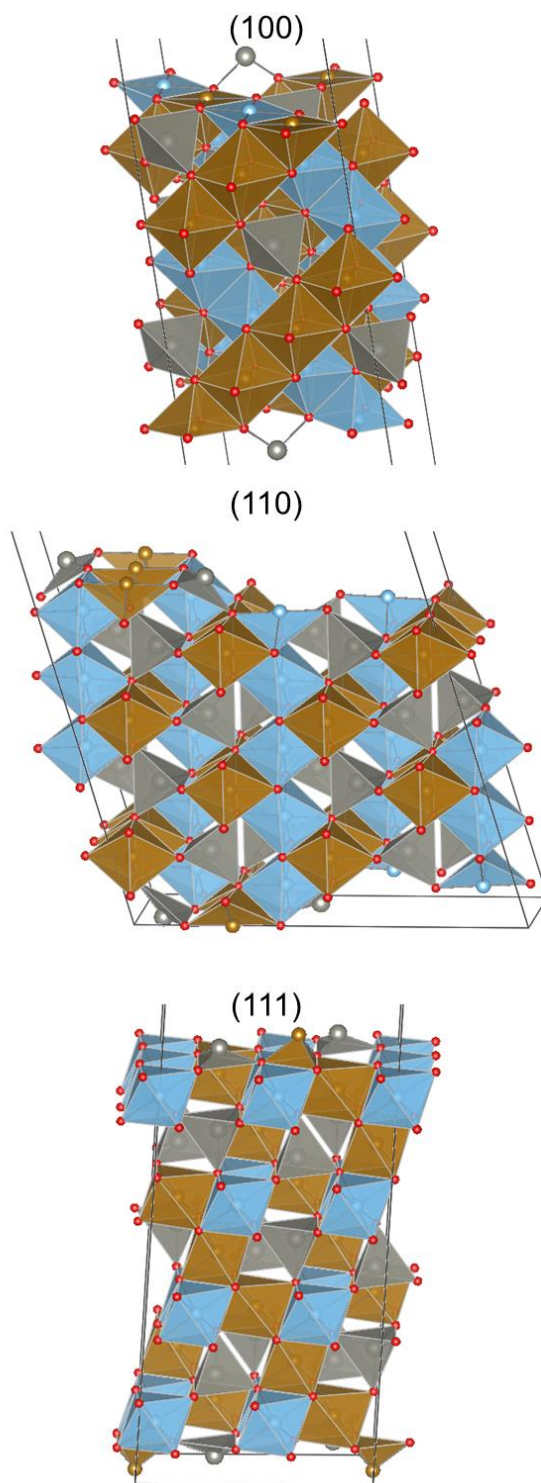


Fig. 1. Terminations of ZnM_2O_4 surfaces. Gray, brown, blue, and red balls indicate Zn, spin-up M, spin-down M, and O. Spin up and down are not distinguished for $\text{M}=\text{Al}$, Ga, In, and Co.

3.2 O vacancy formation

O desorption calculations were conducted with a double supercell of those used in surface calculations without defects. The spacing between defects in these models is anticipated to sufficiently converge defect formation energies based on our previous work²¹. E_{Ovac} for various O sites are shown in Figs. SI-5-12. For the (100) surface, all M are in square pyramidal coordination with five O, and the surface O are at the base of two pyramids. Some surface O additionally bond to Zn, though there is no clear rule relating the value of E_{Ovac} and existence of bonds to Zn from the vacancy site. There are three types of bonding environments in O at the (110) surface: (a) two-fold coordination with a four-fold coordinated M and a four-fold coordinated Zn, (b) three-fold coordination with a four-fold coordinated M, a six-fold coordinated M, and a three-fold coordinated Zn, and (c) three-fold coordination with three six-fold coordinated M. On the other hand, there are three types of bonding environments in O at the (111) surface: (a) three-fold coordination with two six-fold coordinated M and a three-fold coordinated Zn, (b) three-fold coordination with three six-fold coordinated M, and (c) four-fold coordination with a three-fold coordinated M, two six-fold coordinated M, and a three-fold coordinated Zn.

3.2.1 Discussion on smallest E_{Ovac} for each surface

First we discuss the smallest E_{Ovac} for each surface (smallest E_{Ovac}) because the minimum E_{Ovac} site is where reactions are most likely to occur. Figure 2 plots the lowest E_{Ovac} for each surface versus various quantities that can be obtained without explicit defect calculations. Figure 2a shows the smallest E_{Ovac} versus E_{surf} where points for the same M are connected with lines. The difference in E_{Ovac} between the most stable and least stable surfaces span as much as 3.6 eV in ZnGa_2O_4 , strongly indicating that the surface stability must be specified when discussing the smallest E_{Ovac} of the same material. E_{surf} is smallest for the (100) surface (red point is leftmost) for all M, while the smallest E_{Ovac} is largest in the (100) surface (red point is highest) for all compounds except for ZnCo_2O_4 . Connected points for the same M goes down toward the right side with the exception of ZnCo_2O_4 , indicating that the smallest E_{Ovac} of a surface of a material tends to be larger if the surface energy is lower. This finding is reasonable because less stable surfaces would have sites that are in more awkward environments and therefore vulnerable to removal. The points align along a concave curve rather than a straight line. Figure 2b shows the smallest E_{Ovac} versus BG. A decent correlation with the smallest E_{Ovac} and BG is visible in the (100) and (110) surfaces of zinc spinels though ZnV_2O_4 is an outlier. A close observation of the electronic structure of ZnV_2O_4 reveals that there are substantial contributions from O at the bottom of the conduction band in the investigated zinc spinels except for ZnV_2O_4 where the conduction band minimum (CBM) is V $3d(t_{2g})$

states at 0.6 eV from the valence band maximum (VBM) (Figs. SI-13-14). An assumption is made that two bands between 0 eV and 2 eV above the VBM are purely V majority spin $3d$ (t_{2g}) bands and the lowest O states in the conduction band overlaps with states in the V minority spin $3d$ (t_{2g}) band about 2.1 eV from the VBM. Using a correction of 1.5 eV in the CBM of ZnV_2O_4 , which effectively sets the CBM at the V minority spin $3d$ band minimum, the BG becomes 2.1 eV and the smallest E_{Ovac} of 4.2 eV/defect in ZnV_2O_4 becomes in line with the trend formed by other zinc spinels (this correction is applied in empty symbols in Figs. 2b,d,f). E_{Ovac} for the (111) ZnAl_2O_4 and ZnGa_2O_4 surfaces appear to be outliers that are too low in Fig. 2b-d, but the reason is not clear. Plots of the smallest E_{Ovac} versus E_{bulk} , EA, IP, and the work function (WF), which is the mean average of the IP and EA, are given in Figs. 2c-f, respectively.

The correlation between smallest E_{Ovac} of a surface and other quantities can be quantified using the coefficient of determination (R^2) as shown in Table 3. The (100) and (110) surfaces showed a decent correlation ($R^2 > 0.5$) between the smallest E_{Ovac} and E_{bulk} as well as EA. $R^2 < 0.5$ for BG, but the corrected BG when the CBM of ZnV_2O_4 was taken at the V minority spin $3d$ band minimum (BG') satisfies $R^2 > 0.5$. Here, E_{bulk} , EA, and BG are the three quantities with $R^2 > 0.5$ in our previous study on binary oxides²¹, and a good correlation between the surface anion vacancy and E_{bulk} was found in group 3 to 5 hydrides, carbides, and nitrides⁵⁹. On a side note, the bulk O vacancy formation energy of oxides could be modeled by a linear combination of the enthalpy of formation, O $2p$ band center, band gap, and electron negativity difference between cation and anion⁶⁰. In contrast, only the IP and WF have $R^2 > 0.5$ in the (111) surface where the smallest E_{Ovac} of ZnAl_2O_4 and ZnGa_2O_4 is very low compared to what is expected from the trend with E_{bulk} , EA, and BG from other M. The largest R^2 (0.86) in Table 3 is between the smallest E_{Ovac} and IP of the IP (111) surface, which is difficult to explain based on chemical intuition.

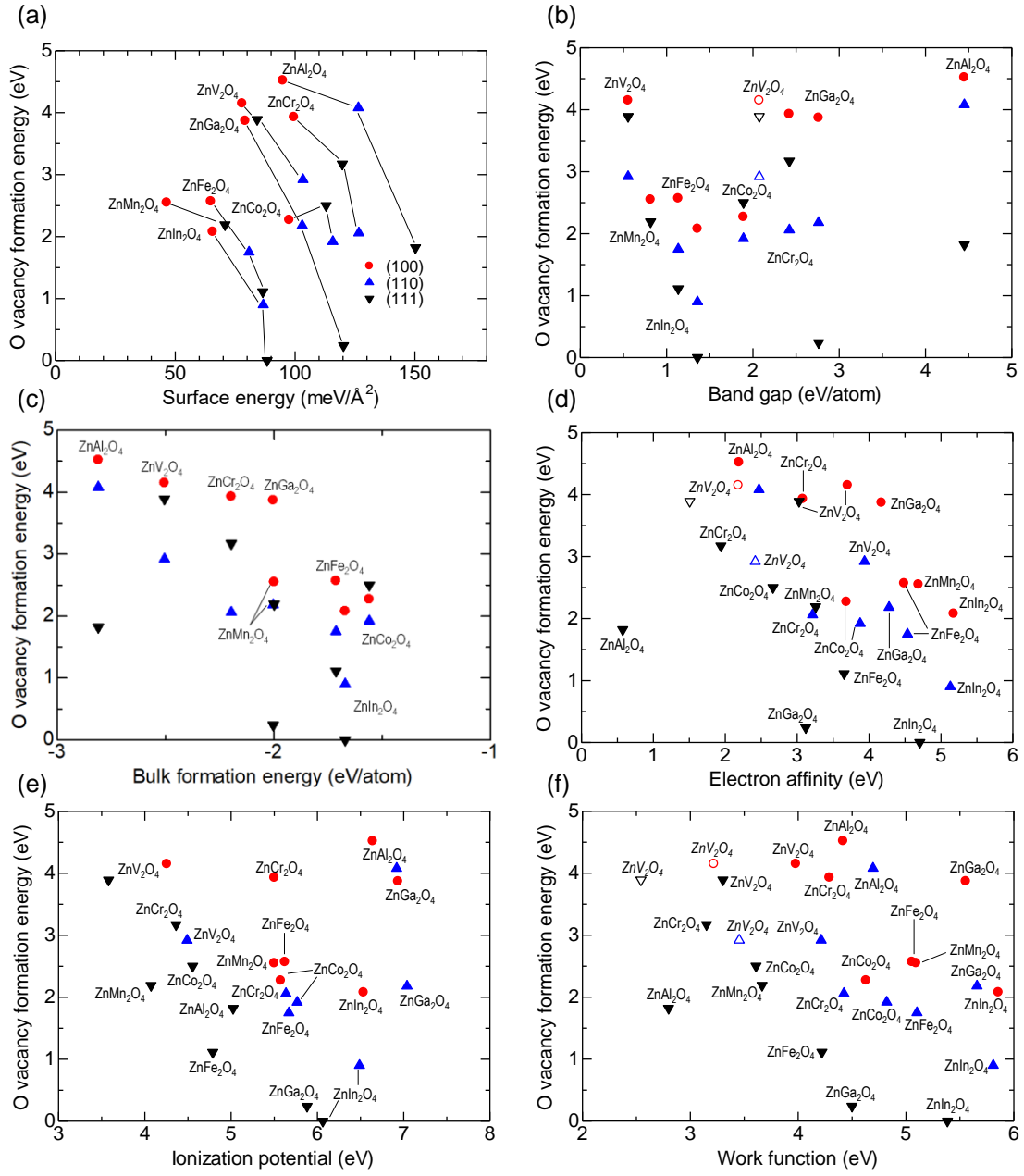


Fig. 2. (a) E_{surf} , (b) minimum BG, (c) E_{bulk} , (d) EA, (e) IP, and (f) WF versus the smallest E_{Ovac} of a surface. The empty symbols in (b,d,f) is when the V minority spin $3d(t_{2g})$ band bottom is taken as the CBM in ZnV_2O_4 .

Table 3. Coefficient of determination (R^2) of the smallest E_{Ovac} versus other quantities. Primed values are when the V minority spin $3d(t_{2g})$ band bottom is taken as the CBM in ZnV_2O_4 .

Surface	BG	BG'	E_{surf}	E_{bulk}	EA	EA'	IP	WF	WF'
(100)	0.31	0.64	0.25	0.81	0.59	0.69	0.00	0.34	0.34
(110)	0.37	0.74	0.38	0.80	0.72	0.76	0.00	0.34	0.30
(111)	0.04	0.00	0.00	0.19	0.20	0.44	0.86	0.64	0.78

3.2.1 Discussion on all E_{Ovac} for each surface and element M

We turn to discussion on relations regarding all O vacancy sites. Figure 3 shows the E_{Ovac} for all surface O sites and all ZnM_2O_4 plotted against E_{bulk} of ZnM_2O_4 . Different symbols are used for different orientations. The R^2 for all points is 0.36, and a higher E_{Bulk} tends to result in a higher E_{Ovac} , which is a trend also found in binary oxides.²¹ The correlation between E_{Ovac} and E_{bulk} strongly depends on the orientation; R^2 is highest in (100) at 0.78, relatively high in (111) at 0.54, and lowest in (111) at 0.18. E_{bulk} had the highest feature importance in (100) and (110) but not in (111) for smallest E_{Ovac} in each ZnM_2O_4 , which is the same trend as the R^2 for all E_{Ovac} .

There is an obvious site environment dependence on E_{Ovac} in (110) and (111). As shown in Figs. SI-5-12, two-fold coordinated O sites at the (110) surface have lower E_{Ovac} than three-fold coordinated sites. The absolute value of the difference between the average E_{Ovac} of three-fold and two-folds coordinated O sites lie between 0.86 to 1.88 eV (in In and Ga, respectively). The percentage of the difference of two-fold sites against three-fold sites is between 28% to 48% (in Al and Ga, respectively). Similarly, the average E_{Ovac} of four-fold coordinated O sites at the (111) surface is 0.06 to 1.67 eV (in V and Ga, respectively) higher than the average of three-fold coordinated O sites. The range of the percentage is 1 to 356% (V and Ga, respectively). The geometrical contribution to the E_{Ovac} of the (111) surface, namely the effect of coordination number, therefore differs widely over the species of M in ZnM_2O_4 in (111), resulting in the lower correlation between E_{Ovac} and E_{bulk} . The correlation between E_{Ovac} and E_{bulk} ignores all site-dependent contributions, thus large scattering between species of M in the geometrical contribution should result in a low correlation. In contrast. the ratio of E_{Ovac} between two-fold and three-fold coordinated O sites on the (110) surface is mostly the same between species of M, thus the site-dependent contributions mostly cancel out and result in a much larger R^2

between E_{Ovac} and E_{bulk} when compared to the (111) surface (Fig. 3). There is a trend in the relation between the position of M in the periodic table and E_{Ovac} ; E_{bulk} increases (absolute value decreases) and E_{Ovac} tends to decrease as the row number increases in group 13 elements and as the group number increases in 3d elements.

The relations between site descriptors and the E_{Ovac} in ZnAl_2O_4 and ZnCr_2O_4 are shown in Fig. 4. The absolute value of the Bader charge, as obtained by the bader code⁶¹⁻⁶⁴, the average bond length, and the coordination number of the desorbing O site were considered as site descriptors. Although a comparison of Bader charge against E_{Ovac} for all O sites over all orientation and all ZnM_2O_4 is very tempting, this is actually a very bad idea. When pseudopotentials are used, as in this study, the Bader volume strongly depends on the number of valence electrons in each element. In an extreme case, using n valence electrons for an atom with a nominal valence of $+n$ results in a nominal charge density of zero for the atom. In such a case, the Bader volume could be zero. However, adding additional valence electrons results in a peak in charge density near the center of the atom, resulting in a non-zero Bader volume. Using the charge density of all electrons is another option, but the total number of electrons based on charge integration tend to differ from the intended number. The reason is a drastic change in the charge density near the nuclei that is difficult to integrate for heavy elements; avoiding this problem is a strong motivation to use pseudopotentials. The choice of pseudopotential is expected to cancel out for the same compound. In contrast, the average bond length and O coordination number are transferrable descriptors that can be used for any system. The results for Bader charge, average bond length, and O coordination number are shown in Figs. SI-15-17, respectively. The average O-Zn bond length could not be used as a descriptor because there are no O-Zn bonds in some O sites. Needless to say, E_{bulk} and other bulk descriptors are the same for all O sites in the same ZnM_2O_4 , therefore cannot be used. The goodness of correlation between E_{Ovac} and site descriptor differed significantly over different ZnM_2O_4 , and Figs. 4(a,c,e) show plots of ZnAl_2O_4 with very bad correlation and Figs. 4(b,d,f) are plots of ZnCr_2O_4 with good correlation.

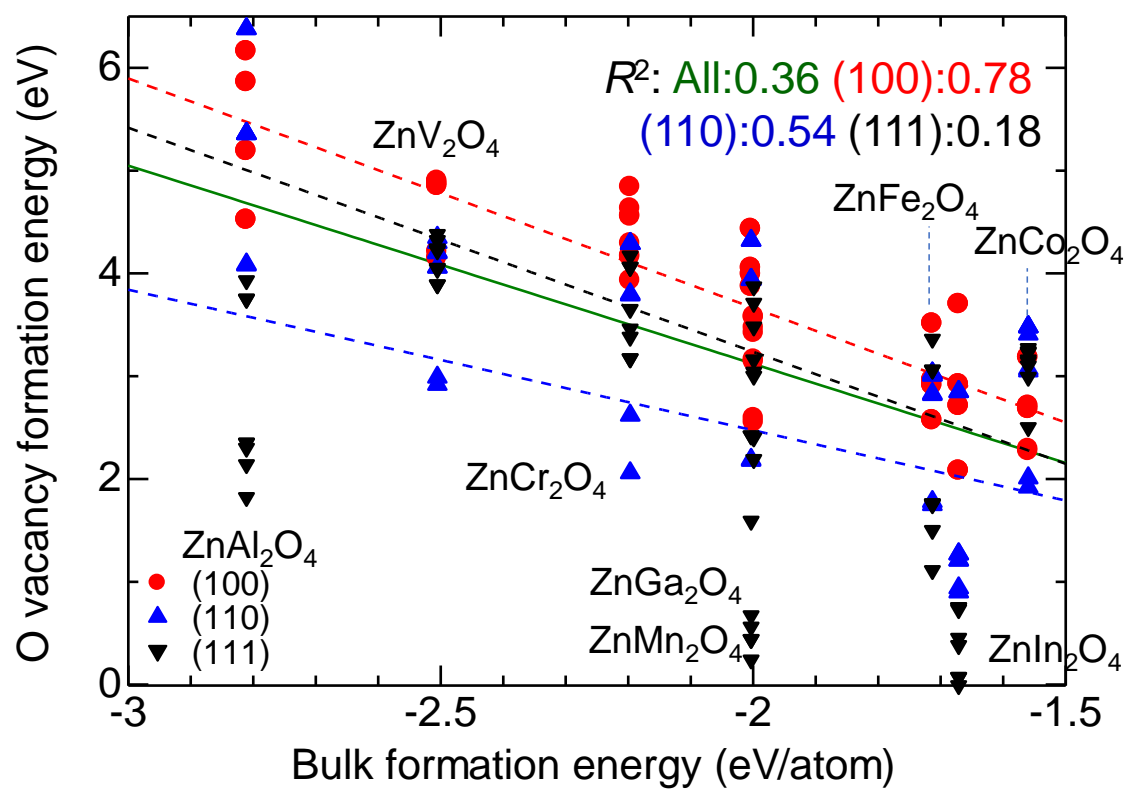


Fig. 3. E_{Ovac} for all surface O sites and all ZnM_2O_4 plotted against E_{bulk} of ZnM_2O_4 .

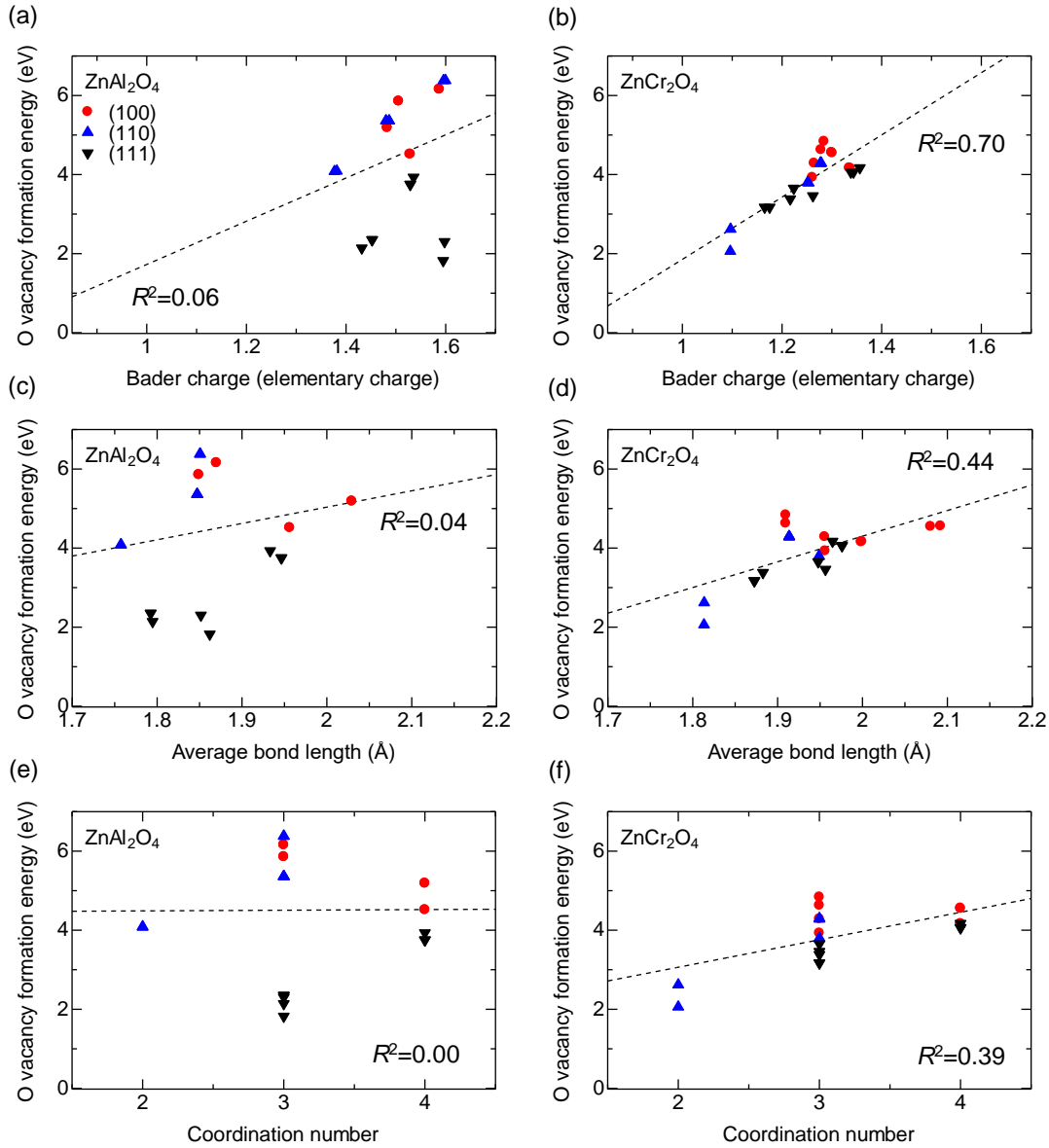


Fig. 4. E_{Ovac} versus (a,b) O site Bader charge, (c,d) average bond length, and (e,f) coordination number of desorbing O for (a,c,e) ZnAl_2O_4 and (b,d,f) ZnCr_2O_4 .

In all ZnM_2O_4 , the trend was a smaller E_{Ovac} when the Bader charge was small (closer to zero), bond length was small, and coordination number was small. Removing an O anion as neutral species forces excitation of atoms in the valence band to a defect state above the VBM. A small Bader charge is therefore qualitatively consistent with a smaller E_{Ovac} because a smaller amount of charge is excited, requiring less energy than when more charge must be excited. The coordination number is expected to correlate with

E_{Ovac} because desorption after severing fewer bonds should result in a lower desorption energy than sites with more bonds, which are sites with higher coordination number. The low correlation of the coordination number and E_{Ovac} could be attributed to the small number of coordination number choices (two for every orientation) and the existence of additional factors that determine E_{Ovac} . We could not suggest a reason for a direct link between bond length and E_{Ovac} . However, the bond length and coordination number have a high R^2 of between 0.60 in ZnCo_2O_4 and 0.84 in ZnFe_2O_4 , where a lower coordination number tends to reduce the average bond length. This is reasonable because a lower coordination number is expected to strengthen each bond and therefore shorten bond lengths. The bond length is thereby effectively acting as a descriptor of the coordination environment. Shorter bond lengths represent a smaller coordination number that need to be severed and, therefore, smaller E_{Ovac} .

Use of further geometrical descriptors may appear interesting but are difficult to implement. An ideal geometrical descriptor reflects the entire coordination environment in some form rather than a limited aspect of the coordination, such as minimum, maximum, difference between maximum-minimum, or average bond length or bond angle. The distortion of the coordination was identified as a good geometrical descriptor of E_{Ovac} in three-fold coordinated O in $\theta\text{-Al}_2\text{O}_3$ and $\beta\text{-Ga}_2\text{O}_3$. This distortion is a single quantity that incorporates information of all bond lengths and angles and therefore reflects the three-dimensional coordination environment. The basic idea is that a large distortion of the coordination environment from an ideal sp^2 or sp^3 coordination makes the O site relatively unstable and therefore decreases E_{Ovac} .⁶⁵ However, O in ZnM_2O_4 bonds with tetrahedrally coordinated Zn and octahedrally coordinated M, thus the coordination environment is much more complicated. As a result, we compromised with the average bond length, which actually did have some correlation with E_{Ovac} , as a descriptor containing information on all bond lengths.

Finally, statistical analysis based on machine learning (ML) techniques were also carried out to predict E_{Ovac} for all the surface O sites of ZnM_2O_4 and identify the important factors for their prediction. Descriptors discussed above such as E_{bulk} , IP, EA, BG, and geometrical descriptors were used. Types of the surface orientations were also implemented using a one-hot encoding method, one example is the Surface(111) descriptor, which is 1 for an O vacancy on the (111) surface and 0 otherwise. Evaluations of well-performing ML methods were performed with a set of six widely used ML methods including three major categories: linear methods for linear regression, kernel methods and tree ensemble methods for nonlinear regression. More specifically, we tested least absolute shrinkage and selection operator (LASSO) and ordinary linear squares

(OLS) regressions as linear methods, support vector regression (SVR) and Gaussian process regression (GPR) as kernel methods, and random forest regression (RFR) and extra trees regression (ETR) as tree ensemble methods. To evaluate the predictive capability of the ML models, Monte Carlo cross validation with 100 times of random leave-10%-out trials was performed to obtain the average root-mean-square error (RMSE). Figure 5 demonstrates that the six ML methods tested in this study could predict the E_{Ovac} within RMSE of 0.49-0.77 eV/defect. Tree ensemble methods predicted relatively well and ETR gave the best predictive accuracy among the models tested. The R^2 value was also calculated to be 0.82 for this ML model based on ETR. This result demonstrates that E_{Ovac} can be predicted by using only 106 datapoints as a dataset and readily available descriptors. The accuracy can be improved once more data are calculated in the future.

With the best ML method (ETR) in hand, the Shapley additive explanations (SHAP) method (version 0.37.0)⁶⁶⁻⁶⁸ was used to identify and prioritize descriptors, as shown in Fig. 6. Namely, contribution of a given input feature to the target (E_{Ovac}) response was identified. The most important descriptor was E_{bulk} , followed by the type of the surface orientation (Surface(111)), IP, coordination numbers and bond length average. As expected, E_{bulk} is a very important descriptor, and the Surface(111) descriptor has a high contribution because, unlike the other two surfaces, the (111) surface has low correlation between E_{Ovac} and E_{bulk} (see Fig. 3 and Table 3). The IP has a good correlation with the smallest E_{Ovac} in the (111) surface, but not in (100) and (111) (see Table 3). The analysis also revealed that E_{Ovac} (SHAP value) tends to be high when E_{bulk} (feature value) is low. This result indicates that information on not only bulk properties but also local structures of the surface O sites is necessary. In addition, both electronic and geometrical properties were found to be important for predicting E_{Ovac} . As an added note, Surface(111) is a discrete, one-hot descriptor, thus points are shown in one of two colors (red and blue) in Fig. 6. However, the SHAP value is the contribution to the output, and therefore is not discrete

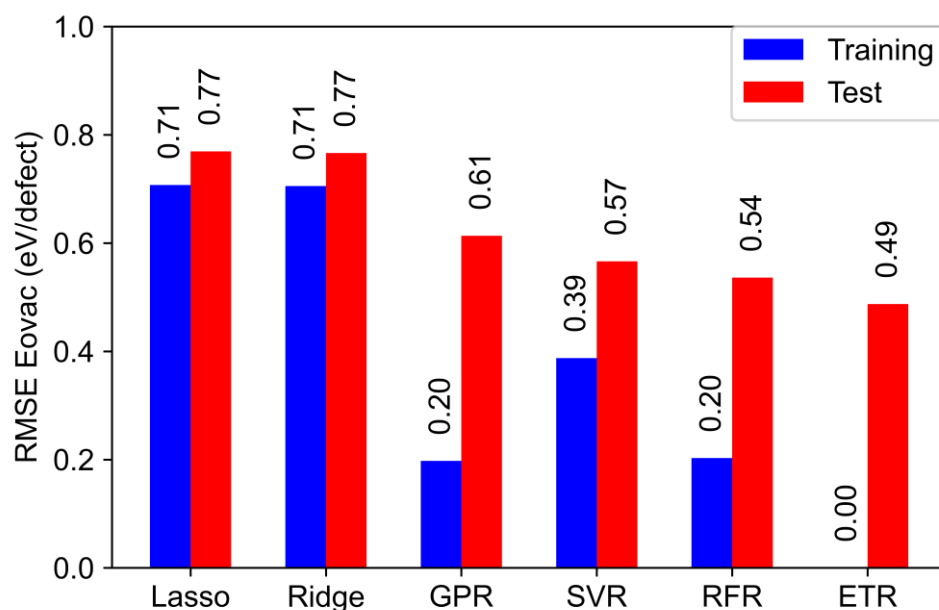


Fig. 5. Average RMSEs for predicting E_{Ovac} for all the surface O sites of ZnM_2O_4 by 100 times of random leave-10%-out trials with various ML methods.

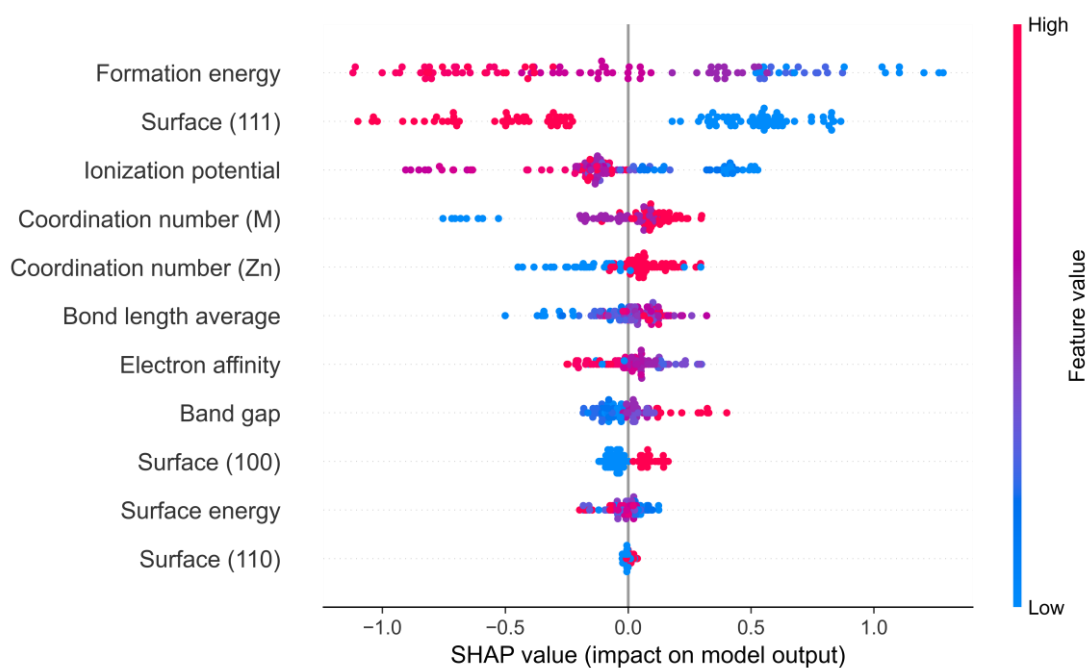


Fig. 6. SHAP values of the descriptors in predicting E_{Ovac} using ETR. SHAP values for individual factors are plotted as dots (blue corresponds to low features, red to high features). Here, features are ordered in descending order according to the sum of the absolute values of the SHAP values.

In summary, a general trend of higher E_{Ovac} with smaller E_{bulk} was observed regardless of the orientation and O desorption site. The quantity E_{bulk} could be a good descriptor of the surface anion desorption energy in not only oxides but in other compounds because E_{bulk} is related to the bond strength between cations and anions and severing of such bonds is necessary to remove surface anions^{21,59}. The Bader charge and the average bond length of an O site could act as a good descriptor of E_{Ovac} , regardless of orientation, in some systems. However, the E_{Ovac} may be strongly off-trend in specific coordination environments that need to be evaluated case-by-case.

4. Conclusions

The E_{Ovac} for various surface orientations of eight normal zinc-based spinel oxides ZnM_2O_4 (M is one of Al, Ga, In, V, Cr, Mn, Fe, or Co) were systematically evaluated and the correlation between physical quantities such as E_{bulk} , BG, and EA were investigated. A large variation of up to 3.6 eV in the smallest E_{Ovac} of a surface was observed for different orientations of same material. E_{Ovac} was typically higher in a more stable surface within the same compound, which is in line with chemical intuition. A good correlation between E_{Ovac} and E_{bulk} , BG, and EA was obtained between the same orientation for (100) and (110) surfaces, although the trend for the (111) surface was contradictory and the IP was more important. These characteristics were reflected in machine learning of E_{Ovac} of all surface sites in all orientations and all compounds. The E_{bulk} , a Boolean descriptor on whether the surface is (111), and the IP were identified as important descriptors, followed by geometrical descriptors that are different in each O site.

Acknowledgments

This study was funded by a grant (No. JPMJCR17J3) from CREST of the Japan Science and Technology Agency (JST), and by a Kakenhi Grant-in-Aid (No. 18K04692) from the Japan Society for the Promotion of Science (JSPS). Computing resources of the Research Institute for Information Technology at Kyushu University, ACCMS at Kyoto University, and the Supercomputer Center in the Institute for Solid State Physics at the University of Tokyo were used. The VESTA code⁶⁹ was used to draw Fig. 1 and Supplementary Figs. SI-1-12.

References

1. G. Pacchioni, *ChemPhysChem*, 2003, **4**, 1041-1047.
2. A. A. Emery, J. E. Saal, S. Kirklin, V. I. Hegde and C. Wolverton, *Chem. Mater.*, 2016, **28**, 5621-5634.
3. F. Oba, M. Choi, A. Togo and I. Tanaka, *Sci. Technol. Adv. Mater.*, 2011, **12**, 034302-034302.
4. C. Freysoldt, B. Grabowski, T. Hickel, J. Neugebauer, G. Kresse, A. Janotti and C. G. Van De Walle, *Rev. Mod. Phys.*, 2014, **86**, 253-305.
5. M. Setvín, M. Wagner, M. Schmid, G. S. Parkinson and U. Diebold, *Chem. Soc. Rev.*, 2017, **46**, 1772-1784.
6. M. V. Ganduglia-Pirovano, A. Hofmann and J. Sauer, *Surf. Sci. Rep.*, 2007, **62**, 219-270.
7. G. Kumar, S. L. J. Lau, M. D. Krcha and M. J. Janik, *ACS Catalysis*, 2016, **6**, 1812-1821.
8. H.-Y. Su, X. Ma, K. Sun, C. Sun, Y. Xu and F. Calle-Vallejo, *Chem. Sci.*, 2020, **11**, 4119-4124.
9. H. Lee, O. Gwon, K. Choi, L. Zhang, J. Zhou, J. Park, J.-W. Yoo, J.-Q. Wang, J. H. Lee and G. Kim, *ACS Catal.*, 2020, **10**, 4664-4670.
10. P. Zhao, M. Ehara, A. Satsuma and S. Sakaki, *J. Catal.*, 2021, **393**, 30-41.
11. G. Pacchioni and H. Freund, *Chem. Rev.*, 2013, **113**, 4035-4072.
12. S. Agarwal, X. Zhu, E. J. M. Hensen, L. Lefferts and B. L. Mojet, *J. Phys. Chem. C*, 2014, **118**, 4131-4142.
13. K. Honkala, *Surf. Sci. Rep.*, 2014, **69**, 366-388.
14. J. Haubrich, E. Kaxiras and C. M. Friend, *Chemistry - A European Journal*, 2011, **17**, 4496-4506.
15. A. R. Albuquerque, A. Bruix, I. M. G. Dos Santos, J. R. Sambrano and F. Illas, *J. Phys. Chem. C*, 2014, **118**, 9677-9689.
16. M. Rellán-Piñeiro and N. López, *J. Phys. Chem. Lett.*, 2018, **9**, 2568-2573.
17. M. Gerosa, C. E. Bottani, L. Caramella, G. Onida, C. Di Valentin and G. Pacchioni, *J. Chem. Phys.*, 2015, **143**, 134702-134702.
18. C. F. Dickens and J. K. Nørskov, *J. Phys. Chem. C*, 2017, **121**, 18516-18524.
19. C. Linderälv, A. Lindman and P. Erhart, *J. Phys. Chem. Lett.*, 2018, **9**, 222-228.
20. W.-J. Yin, S.-H. Wei, M. M. Al-Jassim and Y. Yan, *Appl. Phys. Lett.*, 2011, **99**, 142109.
21. Y. Hinuma, T. Toyao, T. Kamachi, Z. Maeno, S. Takakusagi, S. Furukawa, I. Takigawa and K. Shimizu, *J. Phys. Chem. C*, 2018, **122**, 29435-29444.
22. Q. Zhao, Z. Yan, C. Chen and J. Chen, *Chem. Rev.*, 2017, **117**, 10121-10211.
23. X. Wang, Z. Pan, X. Chu, K. Huang, Y. Cong, R. Cao, R. Sarangi, L. Li, G. Li and S. Feng, *Angew. Chem. Int. Ed.*, 2019, **58**, 11720-11725.
24. Y. Sun, H. Liao, J. Wang, B. Chen, S. Sun, S. J. H. Ong, S. Xi, C. Diao, Y. Du, J.-O. Wang, M. B. H. Breese, S. Li, H. Zhang and Z. J. Xu, *Nat. Catal.*, 2020, **3**, 554-563.
25. A. Rushiti, C. Hättig, B. Wen and A. Selloni, *J. Phys. Chem. C*, 2021, **125**, 9774-9781.

26. A. Ye, Z. Li, J. Ding, W. Xiong and W. Huang, *ACS Catal.*, 2021, DOI: 10.1021/acscatal.1c02742, 10014-10019.
27. F. Zasada, J. Gryboś, P. Indyka, W. Piskorz, J. Kaczmarczyk and Z. Sojka, *J. Phys. Chem. C*, 2014, **118**, 19085-19097.
28. Z. Wang, K. Teramura, S. Hosokawa and T. Tanaka, *J. Mater. Chem. A*, 2015, **3**, 11313-11319.
29. C. Wei, Z. Feng, G. G. Scherer, J. Barber, Y. Shao-Horn and Z. J. Xu, *Adv. Mater.*, 2017, **29**, 1606800.
30. X. Liu, M. Wang, C. Zhou, W. Zhou, K. Cheng, J. Kang, Q. Zhang, W. Deng and Y. Wang, *Chem. Commun.*, 2018, **54**, 140-143.
31. J. Zhang, M. Zhang, S. Chen, X. Wang, Z. Zhou, Y. Wu, T. Zhang, G. Yang, Y. Han and Y. Tan, *Chem. Commun.*, 2019, **55**, 973-976.
32. X. Cui, P. Gao, S. Li, C. Yang, Z. Liu, H. Wang, L. Zhong and Y. Sun, *ACS Catal.*, 2019, **9**, 3866–3876
33. A. M. Bahmanpour, F. Héroguel, M. Kılıç, C. J. Baranowski, P. Schouwink, U. Röthlisberger, J. S. Luterbacher and O. Kröcher, *Appl. Catal. B: Environmental*, 2020, **266**, 118669.
34. P. E. Blöchl, *Phys. Rev. B*, 1994, **50**, 17953-17979.
35. G. Kresse and J. Furthmüller, *Phys. Rev. B*, 1996, **54**, 11169-11186.
36. G. Kresse and D. Joubert, *Phys. Rev. B*, 1999, **59**, 1758-1775.
37. J. P. Perdew, A. Ruzsinszky, G. I. Csonka, O. A. Vydrov, G. E. Scuseria, L. A. Constantin, X. Zhou and K. Burke, *Phys. Rev. Lett.*, 2008, **100**, 136406.
38. Y. Hinuma, H. Hayashi, Y. Kumagai, I. Tanaka and F. Oba, *Phys. Rev. B*, 2017, **96**, 094102.
39. J. P. Perdew, K. Burke and M. Ernzerhof, *Phys. Rev. Lett.*, 1996, **77**, 3865-3868.
40. R. Burns, *Mineralogical Applications of Crystal Field Theory*, Cambridge University Press, Cambridge, U.K., 2 edn., 1993.
41. W. Sato, S. Komatsuda, Y. Yamada and Y. Ohkubo, *Phys. Rev. B*, 2014, **90**, 235204.
42. V. Stevanović, S. Lany, X. Zhang and A. Zunger, *Phys. Rev. B*, 2012, **85**, 115104.
43. S. L. Dudarev, G. A. Botton, S. Y. Savrasov, C. J. Humphreys and A. P. Sutton, *Phys. Rev. B*, 1998, **57**, 1505-1509.
44. P. W. Tasker, *J. Phys. C: Solid State Phys.*, 1979, **12**, 4977.
45. Y. Hinuma, Y. Kumagai, F. Oba and I. Tanaka, *Comp. Mater. Sci.*, 2016, **113**, 221-230.
46. Y. Hinuma, T. Kamachi and N. Hamamoto, *Mater. Trans.*, 2020, **61**, 78-87.
47. M. Reehuis, A. Krimmel, N. Büttgen, A. Loidl and A. Prokofiev, *Eur. Phys. J. B*, 2003, **35**, 311-316.
48. S. K. Sampath and J. F. Cordaro, *J. Am. Ceram. Soc.*, 1998, **81**, 649-654.
49. Z. Galazka, S. Ganschow, R. Schewski, K. Irmscher, D. Klimm, A. Kwasniewski, M. Pietsch, A. Fiedler, I. Schulze-Jonack, M. Albrecht, T. Schröder and M. Bickermann, *APL Mater.*, 2019, **7**,

- 022512.
50. V. Shrivastava and R. Nagarajan, *Dalton Trans.* 2020, **49**, 15810-15820.
 51. Z. Mousavi, F. Soofivand, M. Esmacili-Zare, M. Salavati-Niasari and S. Bagheri, *Sci. Rep.*, 2016, **6**, 20071.
 52. M. Y. Nassar, E. A. El-Moety and M. F. El-Shahat, *RSC Advances*, 2017, **7**, 43798-43811.
 53. J. P. Morán-Lázaro, E. S. Guillén-López, F. López-Urías, E. Muñoz-Sandoval, O. Blanco-Alonso, H. Guillén-Bonilla, A. Guillén-Bonilla, V. M. Rodríguez-Betancourt, M. Sanchez-Tizapa and M. D. I. L. Olvera-Amador, *Sensors*, 2018, **18**, 701.
 54. G. Lal, K. Punia, S. N. Dolia and S. Kumar, *AIP Conf. Proc.*, 2018, **1953**, 120021.
 55. A. Manikandan, J. Judith Vijaya, M. Sundararajan, C. Meganathan, L. J. Kennedy and M. Bououdina, *Superlattices Microstruct.*, 2013, **64**, 118-131.
 56. M. Chakraborty, R. Thangavel, A. Biswas and G. Udayabhanu, *CrystEngComm*, 2016, **18**, 3095-3103.
 57. Y. Azoudj, Z. Merzougui, G. Rekhila and M. Trari, *Appl. Water Sci.*, 2018, **8**, 114.
 58. Y. Hinuma, F. Oba, Y. Kumagai and I. Tanaka, *Phys. Rev. B*, 2012, **86**, 245433.
 59. Y. Hinuma, S. Mine, T. Toyao, Z. Maeno and K.-i. Shimizu, *Phys. Chem. Chem. Phys.*, 2021, **23**, 16577-16593.
 60. A. M. Deml, A. M. Holder, R. P. O'Hayre, C. B. Musgrave and V. Stevanović, *J. Phys. Chem. Lett.*, 2015, **6**, 1948-1953.
 61. G. Henkelman, A. Arnaldsson and H. Jónsson, *Comp. Mater. Sci.*, 2006, **36**, 354-360.
 62. E. Sanville., S. D. Kenny, R. Smith and G. Henkelman, *J. Comput. Chem.*, 2007, **28**, 899-908.
 63. W. Tang, E. Sanville and G. Henkelman, *J. Phys.: Condens. Matter*, 2009, **21**, 084204.
 64. M. Yu and D. R. Trinkle, *J. Chem. Phys.*, 2011, **134**, 064111.
 65. Y. Hinuma, T. Kamachi, N. Hamamoto, M. Takao, T. Toyao and K.-i. Shimizu, *J. Phys. Chem. C*, 2020, **124**, 10509-10522.
 66. S. M. Lundberg and S.-I. Lee, presented in part at the Proceedings of the 31st International Conference on Neural Information Processing Systems, Long Beach, California, USA, 2017.
 67. S. M. Lundberg, G. Erion, H. Chen, A. DeGrave, J. M. Prutkin, B. Nair, R. Katz, J. Himmelfarb, N. Bansal and S.-I. Lee, *Nat. Machine Intelligence*, 2020, **2**, 56-67.
 68. S. Mine, M. Takao, T. Yamaguchi, T. Toyao, Z. Maeno, S. M. A. Hakim Siddiki, S. Takakusagi, K.-i. Shimizu and I. Takigawa, *ChemCatChem*, 2021, **13**, 3636-3655
 69. K. Momma and F. Izumi, *J. Appl. Crystallogr.*, 2011, **44**, 1272-1276.